Editors' Suggestion | Featured in Physics

Extended Spatial Coherence of Interlayer Excitons in $MoSe_2/WSe_2$ Heterobilayers

Mirco Troue,[1,2,*] Johannes Figueiredo,[1,2,*] Lukas Sigl,[1,2] Christos Paspalides,[1,2] Manuel Katzer,[3] Takashi Taniguchi,[4] Kenji Watanabe,[5] Malte Selig,[3] Andreas Knorr,[3] Ursula Wurstbauer,[6] and Alexander W. Holleitner[1,2,†]

[1]*Walter Schottky Institute and Physics Department, Technical University of Munich, Am Coulombwall 4a, 85748 Garching, Germany*

[2]*Munich Center for Quantum Science and Technology (MCQST), Schellingstr. 4, 80799 Munich, Germany*

[3]*Institute for Theoretical Physics, Nonlinear Optics and Quantum Electronics, Technical University of Berlin, 10623 Berlin, Germany*

[4]*Research Center for Materials Nanoarchitectonics, National Institute for Materials Science, 1-1 Namiki, Tsukuba 305-0044, Japan*

[5]*Research Center for Electronic and Optical Materials, National Institute for Materials Science, 1-1 Namiki, Tsukuba 305-0044, Japan*

[6]*Institute of Physics, Münster University, Wilhelm-Klemm-Str. 10, 48149 Münster, Germany*

(Received 17 February 2023; accepted 9 June 2023; published 19 July 2023)

We report on the spatial coherence of interlayer exciton ensembles as formed in $MoSe_2/WSe_2$ heterostructures and characterized by point-inversion Michelson-Morley interferometry. Below 10 K, the measured spatial coherence length of the interlayer excitons reaches values equivalent to the lateral expansion of the exciton ensembles. In this regime, the light emission of the excitons turns out to be homogeneously broadened in energy with a high temporal coherence. At higher temperatures, both the spatial coherence length and the temporal coherence time decrease, most likely because of thermal processes. The presented findings point towards a spatially extended, coherent many-body state of interlayer excitons at low temperature.

DOI: 10.1103/PhysRevLett.131.036902

In the rapidly growing family of two-dimensional materials, many-body excitations of charge carriers play an essential role in describing the emergent quantum phenomena in the atomistic materials with ultimately confined dimensions in one direction and a low dielectric screening [1]. Particularly, van der Waals heterostructures of semiconducting two-dimensional materials, such as $MoSe_2$ and WSe_2, are ideal systems to study the many-body phase diagram of interlayer excitons (IXs) [2,3]. The latter are Coulomb-bound electron-hole pairs, where the electron is situated in one layer and the hole in the other layer of a heterostructure. Such excitons are composite bosons and turn out to exhibit a large exciton binding energy of several hundreds of meV, long photoluminescence lifetimes exceeding the thermalization timescales, and a possible gate-tunable interlayer hybridization [4–8]. In order to experimentally verify the emergence of a spatially extended quantum many-body state, the exciton ensembles have to comprise mobile particles such that each exciton can interact, e.g., via dipole-dipole interactions with other excitons in the ensemble [2,3,9,10]. The corresponding free expansion of excitons has been proven for IXs in several geometries and heterostructures [11–16]. Recently, it was demonstrated that IXs can show an enhanced temporal coherence time, i.e., a reduced spectral linewidth in the predicted degeneracy limit where the excitons are supposed to coherently interact with each other [17]. However, it was pointed out in several reports on many-body exciton ensembles [17–24], that it is required to demonstrate the extended spatial coherence of the excitons as an evidence of a coherent many-body state. In this Letter, we demonstrate that the spatial coherence length of IXs in van der Waals $MoSe_2/WSe_2$ heterostructures can reach values equal to the spatial expansion length of the exciton ensembles, when measured in the few Kelvin regime. Our results open the pathway for quantum technological devices based on coherent exciton ensembles with the possibility to integrate them in laterally patterned, logical circuits [25,26].

The investigated samples consist of stacked heterobilayers of $MoSe_2$ and WSe_2 monolayers in an H-type configuration encapsulated in hBN [Fig. 1(a)]. Corresponding photoluminescence spectra show a single Lorentzian emission peak at $E_{IX} = 1.389$ eV ($\lambda_{IX} = 892.6$ nm) at low excitation powers and temperatures [Fig. 1(b)], as consistent with [17,27]. The luminescence can be interpreted to stem from IXs where the electron (hole) is situated in the $MoSe_2$ (WSe_2). The narrow Lorentzian emission line persists down to the lowest investigated excitation powers without separating into distinct lines, and it features a lifetime of several tens of ns. In turn, we interpret the IXs to occupy the lowest excitonic energy state of the corresponding composite-boson

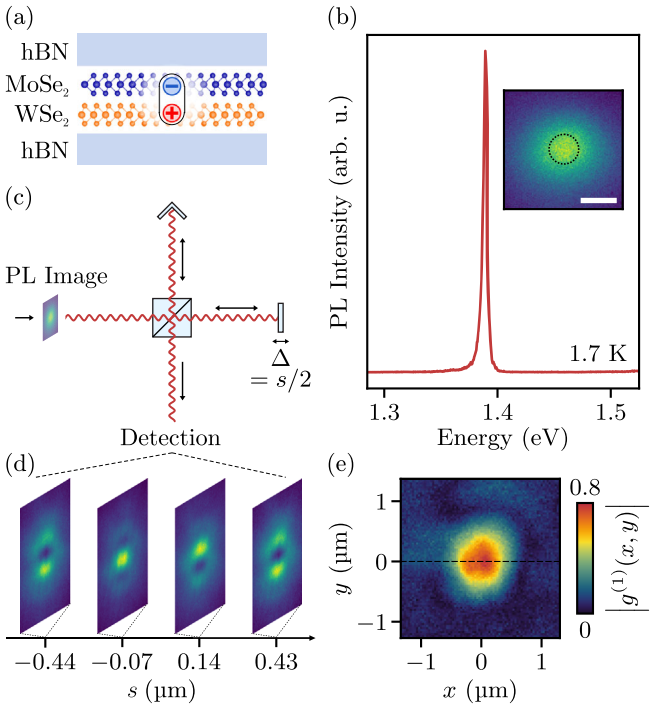

FIG. 1. (a) Sketch of a $MoSe_2/WSe_2$ heterobilayer encapsulated in hBN. (b) Photoluminescence spectrum of corresponding interlayer excitons (IXs) with an emission energy of $E_{IX} = 1.389$ eV ($\lambda_{IX} = 892.6$ nm) at $T_{bath} = 1.7$ K ($E_{laser} = 1.94$ eV and $P_{laser} = 2$ μW). Inset: spatially resolved photoluminescence image of the sample at $P_{laser} = 3$ μW. Scale bar, 1 μm. Dotted circle: measured point spread function (PSF) of the optical circuitry at λ_{IX}. (c) Concept of the point-inversion Michelson-Morley interferometry. (d) Four exemplary interference images of the photoluminescence image as in the inset of (a) vs the path difference $s = 2\Delta$. (e) Corresponding spatially resolved coherence image $|g^{(1)}(x, y)|$.

ensemble. The inset of Fig. 1(b) shows a spatial image of the excitonic photoluminescence $I(x, y)$ vs the coordinates x and y. A clear photoluminescence signal is detected several hundreds of nanometers beyond the measured point spread function (PSF) at λ_{IX}, which amounts to (899 ± 18) nm in the utilized optical circuitry (cf. dotted circle). As a result, we infer that the imaged long-lived IXs propagate hundreds of nanometers within the plane of the studied heterobilayer [11–16].

We perform a point-inversion Michelson-Morley interferometry to characterize the spatial and temporal coherence of the excitonic photoluminescence. Starting points are spatially homogeneous photoluminescence images [inset of Fig. 1(b)]. In the interferometer, a centered 50/50 beam splitter distributes the incoming photoluminescence equally into the two arms [Fig. 1(c)]. In one of them, a three-sided retroreflector point inverts the image, i.e., $I_1(x, y) \rightarrow I_1(-x, -y)$, while in the second arm, a plane mirror reflects the image, $I_2(x, y) \rightarrow I_2(x, y)$. Both, the point-inverted and the unchanged image pass the beam splitter again and interfere with each other in the detection path. The superposition is finally detected and reveals the spatial interference relative to the inversion center [28]. We utilize a piezostepper to move the mirror in the second arm by a distance Δ, which introduces an optical path difference $s = 2\Delta$ and a time delay $\tau = s/c$ between the two paths (with c the speed of light). For each s, we observe interference fringes with a period consistent with the exciton emission wavelength λ_{IX}. Figure 1(d) shows such interference images for $s = -0.44$, -0.07, $+0.14$, and $+0.43$ μm. Per x and y coordinate of the original image, the detected intensity is described as [29]

$$I(\tau, x, y) = I_1 + I_2 + 2 \cdot \sqrt{I_1(0, -x, -y) I_2(\tau, x, y)} \cdot g^{(1)}(\tau, x, y) \cos\left(\frac{2\pi}{\lambda_{IX}} c\tau\right), \quad (1)$$

with $g^{(1)}(\tau, x, y)$ the normalized first-order correlation function given by

$$g^{(1)}(\tau, x, y) = \frac{E(0, -x, -y) \cdot E^*(\tau, x, y)}{\sqrt{I_1(0, -x, -y) I_2(\tau, x, y)}} \quad (2)$$

and $E = E(\tau, x, y)$ the electric field and $E^* = E^*(\tau, x, y)$ its complex conjugate of the interfering photons. In turn, images such as in Fig. 1(d) allow us to determine $|g^{(1)}(\tau, x, y)|$, which is proportional to the visibility of the interference. The latter is limited by the ratio of the light intensities in the two interferometer arms to $2 \cdot [\sqrt{I_1 I_2}/(I_1 + I_2)]$, which we calculate to be 0.98. The limit stems from the fact that the retroreflector in the first arm of the interferometer has a slightly reduced total reflectance compared to the mirror in the second arm. All presented values of $|g^{(1)}(\tau, x, y)|$ are normalized to this technical limit.

The first-order correlation function implies the temporal coherence time of the excitonic photoluminescence, when the time delay τ is varied for $x = y = 0$. Namely, a variation of the optical path difference in the center of the PSF, i.e., the central pixel of the detection spot, introduces the necessary temporal offset between the interfering photoluminescence images. We write $|g^{(1)}(\tau)| = |g^{(1)}(\tau, x = 0, y = 0)|$ and plot $|g^{(1)}(\tau)|$ vs s and therefore τ (Fig. 2). As expected, for $\tau = 0$, $|g^{(1)}(\tau)|$ reaches the maximum value as in Fig. 1(e). Fitting the data with an exponential fit (dashed lines), we determine the maximum to be $|g^{(1)}(\tau = 0)| = 0.76 \pm 0.02$ (=76%), and note that for an excitation at lower power, a value of 88% is observed, as discussed below. The full width at half maximum (FWHM) of the data in Fig. 2 is $\tau_c = (223 \pm 6)$ fs, which is the temporal coherence time of the excitonic photoluminescence. The Lorentzian shape of the investigated photoluminescence spectra, as in Fig. 1(b), warrants the use of the exponential fit in Fig. 2 [29]. For the spectrum underlying the

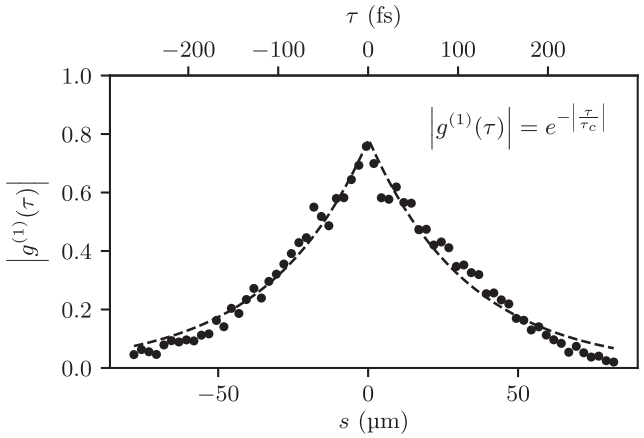

FIG. 2. Normalized first order correlation function $|g^{(1)}(\tau)| = |g^{(1)}(\tau, x = 0, y = 0)|$ as in Fig. 1(e) for $x = 0$, $y = 0$, as a function of s and therefore, $\tau = s/c$, with c the speed of light. The full width at half maximum (FWHM) of $|g^{(1)}(\tau)|$ gives the temporal coherence time $\tau_c = (223 \pm 6)$ fs. The exponential curves fit the data as expected for a purely homogeneously broadened light emission. All experimental parameters as in Fig. 1(e).

measurement of Fig. 2, the energetic photoluminescence linewidth is (5.60 ± 0.04) meV. In turn, a τ_c of (235 ± 17) fs is expected, which agrees with the experimentally determined value in Fig. 2. Correspondingly, the excitonic photoluminescence such as in Fig. 1(b) fulfills the Wiener-Khinchin theorem for a homogeneously broadened emitter [29]. We note that our finding on the temporal coherence time is consistent with an earlier report on similar $MoSe_2/WSe_2$ heterobilayers [17].

Generally, the coherence of exciton ensembles is affected by photo-induced local heating effects and the impact of hot charge carriers and extra excitons [30]. Moreover, a continuous laser excitation permanently induces coherence and enhances the interferometric visibility of the exciton photoluminescence. We therefore use a pulsed laser excitation and detect the excitonic photoluminescence images at a delayed time, such that the laser is turned off and the mentioned extrinsic effects are minimized. Figure 3(a) depicts the total emission of a photoluminescence image, such as the one in the inset of Fig. 1(b), as a function of the time delay after the laser excitation. The image is spectrally integrated in the range $1.378\ \text{eV} \leq E_{\text{photon}} \leq 1.442\ \text{eV}$, with E_{photon} the photoluminescence energy, such that only the exciton emission at $E_{\text{IX}} = 1.389$ eV is detected. The dashed line in Fig. 3(a) is an exponential fit to the data giving the photoluminescence lifetime to be (20.3 ± 1.3) ns for the specific experimental parameters. For the spatial coherence measurements, Fig. 3(b), we choose the detection window with a width of 22.4 ns to start 6.4 ns after the laser pulse. Within the detection window, we determine $|g^{(1)}(\tau = 0, x, y = 0)| = |g^{(1)}(x)|$, i.e., along the x coordinate of the excitonic photoluminescence images [e.g., dashed line in Fig. 1(e)]. To do so, the optical path difference τ is symmetrically varied around zero: $-1.67\ \text{fs} \leq \tau \leq +1.67\ \text{fs}$ $(-0.5\ \mu\text{m} \leq s \leq +0.5\ \mu\text{m})$ and corresponding interference images are analyzed. The already introduced width of the temporal detection window of 22.4 ns is chosen to achieve a high enough signal-to-noise ratio for this analysis. Figure 3(b) depicts the corresponding $|g^{(1)}(x)|$ for several laser powers. For each, we fit $|g^{(1)}(x)|$ with a Gaussian function [dashed lines in Fig. 3(b)] to reveal the FWHM, which is the spatial coherence length x_c of the excitonic emission. Figure 3(c) compares x_c to the PSF for several laser powers. For $P_{\text{laser}} = 200$ nW, we measure a spatial coherence length of $x_c = (1.6 \pm 0.3)$ μm, which significantly exceeds the measured PSF (dotted line), while for high excitation powers,

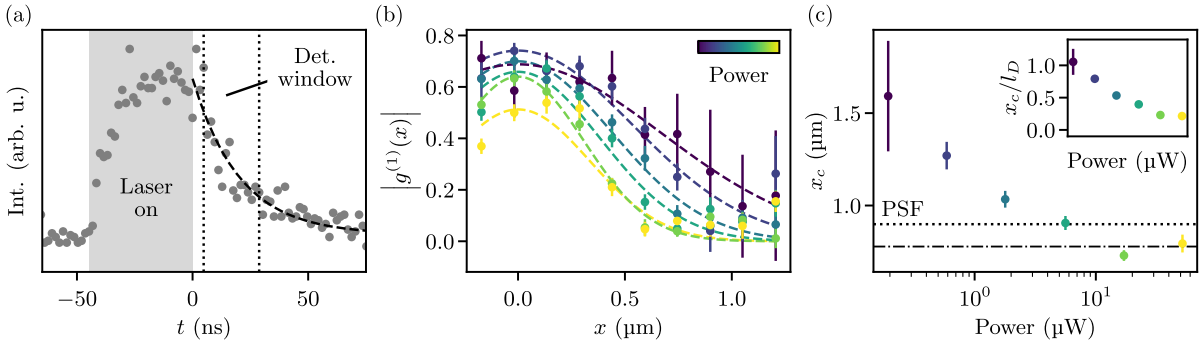

FIG. 3. (a) Time-resolved photoluminescence of IXs at $E_{\text{IX}} = 1.389$ eV. After the laser is turned off, the photoluminescence decays exponentially with a lifetime of (20.3 ± 1.3) ns (dashed line). For the interference experiments, the signal is detected during a time window of 22.4 ns at a time delay of 6.4 ns after the laser is turned off. (b) $|g^{(1)}(x)|$ of the signal within the detection window of (a) for several laser powers vs the spatial coordinate x, i.e., $|g^{(1)}(x)| = |g^{(1)}(\tau = 0, x, y = 0)|$ as highlighted by the dashed line in Fig. 1(e). Dashed lines are Gaussian fits to the data to extract the FWHM of the spatial distributions, which is the spatial coherence length x_c. (c) Dependence of x_c on P_{laser}. At lowest power, x_c exceeds the PSF of the optical circuitry, while for high powers, x_c is consistent with the PSF. Dotted (dotted-dashed) line: PSF at λ_{IX} (at the excitation wavelength). Inset: ratio of x_c to the FWHM l_D of the overall spatial photoluminescence images [cf. inset of Fig. 1(b)].

the data are well described by the PSF. We tentatively explain the decrease of the spatial coherence for high laser powers by the increasing influence of exciton-exciton interactions, e.g., with excitons at higher kinetic energies in the exciton ensembles [32]. For even higher powers, further exciton transitions at higher emission energies eventually start to dominate the photoluminescence spectra (data not shown, since already discussed in [17] on other samples).

In order to compare the spatial coherence length x_c to the lateral expansion of the IXs, we determine the spatial expansion of the excitons by fitting the spatial photoluminescence images, such as in the inset of Fig. 1(b), with two-dimensional Gaussian distributions and define their isotropic FWHM as the excitonic expansion length l_D. Plotting the ratio of x_c vs l_D [inset of Fig. 3(c)], we observe that for the lowest investigated power of 200 nW, x_c reaches the value of the spatial expansion of the exciton ensemble within the plane of the $MoSe_2/WSe_2$ heterobilayer. For high laser powers, the ratio decreases to ~0.2, which can be explained by a transition from a spatially coherent to an incoherent IXs ensemble.

In Fig. 4, we discuss the temperature dependence of the exciton dynamics. Figure 4(a) depicts the photoluminescence spectra for an increasing temperature. Above 10 K, the intensity decreases significantly, while $|g^{(1)}(\tau)|$ deviates from the Lorentzian profile approaching a Gaussian one, and it is not described by double-exponential curves as for below 10 K [Fig. 4(b)]. We note that for the data of Fig. 4(b), $|g^{(1)}(\tau)|$ reaches 0.88 ± 0.03 (88%). The apparent difference to Fig. 2 is explained by a lower excitation power and in turn, by a reduced impact of excess energy at the excitation spot [3 μW in Fig. 2 vs 400 nW in Fig. 4(b)]. Figure 4(c) shows the extracted τ_c vs T_{bath} at this power. For low temperatures, τ_c reaches a value of up to 370 fs. We detect this maximum when the laser is "on" and again, for a low laser power. The value monotonically decreases for the detection being delayed with respect to the laser irradiation (not shown). The gray dashed line in Fig. 4(c) is a guide to the eye. Last but not least, Fig. 4(d) depicts x_c vs T_{bath}, again analyzed for a detection-window when the laser is "off." Within the given uncertainty of the interferometric method, x_c decreases and approximates the PSF for high temperatures, as will be discussed in the following.

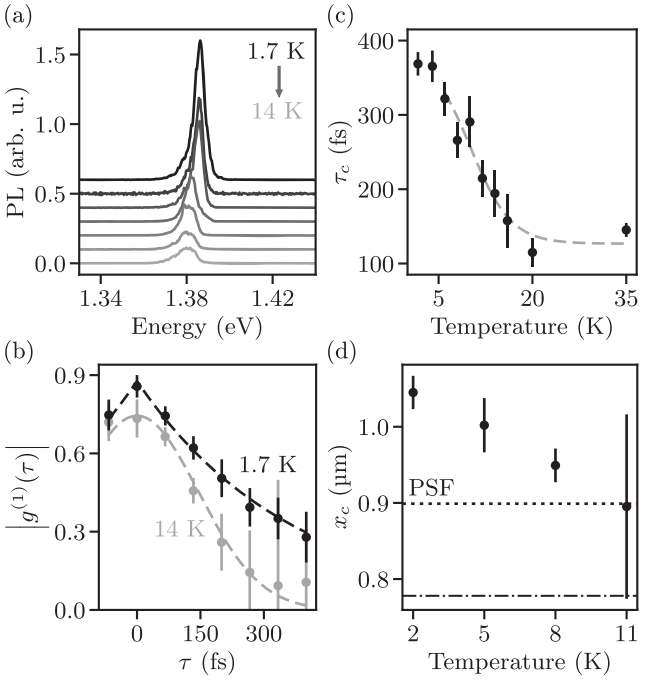

FIG. 4. (a) Photoluminescence spectra of IXs for $T_{\mathrm{bath}} = 1.7, 4, \ldots, 14$ K. (b) Normalized $|g^{(1)}(\tau)|$ for $T_{\mathrm{bath}} = 14$ (gray) and 1.7 K (black). (c) Temporal coherence time τ_c vs T_{bath}. Gray dashed line is a guide to the eye. (d) Spatial coherence length x_c vs T_{bath}. Time delay: 19.2 ns and time window of 16 ns. Dotted line (dotted-dashed line) is the PSF at λ_{IX} (at the excitation wavelength). Experimental parameters are $E_{\mathrm{laser}} = 1.94$ eV and $P_{\mathrm{laser}} = 400$ nW.

Generally, the investigated IX ensembles exhibit spatially homogeneous photoluminescence images [inset of Fig. 1(b)], where the photon emission exceeds the spatial extent of the measured PSF by several hundreds of nanometers. In turn, we infer that at least, a subensemble of the IXs is mobile [11–16]. Significantly, x_c matches l_D at low excitation power [inset of Fig. 3(c) and [30]]. Correspondingly, localization phenomena do not seem to hinder the presented spatial coherence phenomena in the investigated regime [33,34]. We estimate the exciton density to be as high as $\sim 10^{11}$ cm^{-2}, suggesting that the exciton ensembles are degenerate below 10 K [17]. As a result, we assume the underlying exciton expansion to be a quantum mechanical percolation process within the two-dimensional potential landscape [35]. As far as τ_c is concerned, its maximum reaches a value of $\tau_c \sim 370$ fs at low temperature [Fig. 4(c)], which is consistent with [17,36]. Tentatively, we interpret this fast process by a possible momentum and energy transfer during the photon-emission process, because in our current understanding, the IXs are very likely indirect in momentum space [33,37], and every scattering event of the excitons (whether the emission of a photon is involved or not), results in a loss of coherence. Once a photon is emitted, processes such as exciton-phonon scattering lead to a constant refill of the empty states which were emitting into the light cone. However, since the light cone covers only a small energy range, the overall refill mechanism occurs on a longer timescale (ns), since, e.g., acoustic phonons need to be involved. Therefore, the photoluminescence decays on a much slower timescale of a few tens of nanoseconds corresponding to the exciton lifetime [36]. As far as the involved processes are concerned, for low temperatures, a coupling to an underlying low-lying collective excitation of

the exciton ensembles is reasonable [37,38], while for higher temperatures, a thermally activated momentum transfer via phonons is probable. Consistently, above 10 K, we observe that $|g^{(1)}(\tau)|$ can be fitted by Gaussian curves expressing an inhomogeneous broadening [Fig. 4(b)] [29] and that τ_c decreases [Fig. 4(c)]. Both findings suggest that the IXs are in a thermal regime with significantly reduced coherence at elevated temperatures. Figure 4(d) shows x_c vs T_{bath}. We restrict ourselves to the range of $1.7\ \mathrm{K} \leq T_{\mathrm{bath}} \leq 11\ \mathrm{K}$, because above 10 K, the photoluminescence amplitude significantly drops [Fig. 4(a)] and the light emission is increasingly inhomogeneously broadened. For $1.7\ \mathrm{K} \leq T_{\mathrm{bath}} \leq 11\ \mathrm{K}$, x_c decreases [Fig. 4(d)] most likely because of the increased influence of thermally activated processes. At higher temperatures, the noise appearing for x_c increases because of the reduced photoluminescence amplitude [cf. Fig. 4(a)], but the PSF is the natural limit of x_c for higher temperatures [Fig. 4(d)]. So far, we compared the data to the PSF at λ_{IX} which amounts to (899 ± 18) nm [dotted lines in Figs. 1(b), 3(c), and 4(d)], measured as a convolution of the excitation and detection path at this wavelength. The similarly measured PSF at the utilized excitation wavelength of 639 nm is (779 ± 18) nm [dashed-dotted line in Figs. 3(c) and 4(d)]. In turn, we can expect that the excitation spot is on the order of 550 nm ($\sim 779\ \mathrm{nm}/\sqrt{2}$). Consistently, the data in the presumably incoherent regime at high laser power and/or high temperatures lie in-between the two mentioned PSFs [cf. Figs. 3(c) and 4(d)].

Future studies might resolve the transition to single excitons at even lower excitation powers, as was done for IXs in III–V semiconductor double quantum wells [25], and the impact of exciton-exciton and exciton-phonon interactions on the spatial coherence at higher densities and/or lower temperatures in combination with the bosonic and fermionic aspects of interactions [34]. Moreover, the high interference visibility of the IX ensembles is comparable to the one reported for exciton-polaritons in similar heterobilayers (~80% in [28]). In turn, our results suggest the general feasibility of quantum devices based on spatially confined coherent exciton ensembles interacting coherently with photons [12,25,26]. Lastly, for an experimental evidence of an exciton condensation in the momentum space, back-focal plane imaging seems to be suitable, however, at temperatures significantly below 1 K [27], which is beyond the scope of the current study.

In summary, we show that the photoluminescence of IXs, as formed in heterobilayers of $MoSe_2$ and WSe_2 monolayers can exhibit an extended spatial coherence length exceeding the PSF of the utilized optical circuitry below 10 K. The spatial coherence length reaches the spatial extent of the exciton ensemble in the investigated regime, and it decreases to the PSF for increasing laser intensities and/or temperatures. The photoluminescence of the coherent exciton ensemble turns out to exhibit a temporal coherence time of several 100s of femtoseconds and a high interference visibility. We determine the temperature dependence of both the temporal coherence time and the spatial coherence length, suggesting that above 10 K thermal processes start to dominate the exciton interactions fostering the transition to a nondegenerate exciton gas.

We gratefully acknowledge the fruitful discussions with N. Wilson and A. Hartschuh about the exciton dynamics and the imaging geometries as well as the German Science Foundation (DFG) for financial support via Grants HO 3324/9-2, WU 637/4-2 and 7-1, KN 427/11-2, and project No. 18208777 of SFB 951, as well as the clusters of excellence MCQST (EXS-2111) and e-conversion (EXS-2089), and the priority program 2244 (2DMP). K. W. and T. T. acknowledge support from the JSPS KAKENHI (Grants No. 20H00354, No. 21H05233, and No. 23H02052) and World Premier International Research Center Initiative (WPI), MEXT, Japan.

*These authors contributed equally.
†holleitner@wsi.tum.de

[1] N. P. Wilson, W. Yao, J. Shan, and X. Xu, Excitons and emergent quantum phenomena in stacked 2D semiconductors, Nature (London) **599**, 383 (2021).
[2] J. M. Blatt, K. W. Böer, and W. Brandt, Bose-Einstein condensation of excitons, Phys. Rev. **126**, 1691 (1962).
[3] M. M. Fogler, L. V. Butov, and K. S. Novoselov, High-temperature superfluidity with indirect excitons in van der Waals heterostructures, Nat. Commun. **5**, 4555 (2014).
[4] P. Rivera *et al.*, Observation of long-lived interlayer excitons in monolayer $MoSe_2 - WSe_2$ heterostructures, Nat. Commun. **6**, 1 (2015).
[5] B. Miller, A. Steinhoff, B. Pano, J. Klein, F. Jahnke, A. Holleitner, and U. Wurstbauer, Long-lived direct and indirect interlayer excitons in van der Waals heterostructures, Nano Lett. **17**, 5229 (2017).
[6] A. T. Hanbicki, H.-J. Chuang, M. R. Rosenberger, C. S. Hellberg, S. V. Sivaram, K. M. McCreary, I. I. Mazin, and B. T. Jonker, Double indirect interlayer exciton in a $MoSe_2/WSe_2$ van der Waals heterostructure, ACS Nano **12**, 4719 (2018).
[7] P. Merkl *et al.*, Ultrafast transition between exciton phases in van Der daals heterostructures, Nat. Mater. **18**, 691 (2019).
[8] J. Kiemle, F. Sigger, M. Lorke, B. Miller, K. Watanabe, T. Taniguchi, A. Holleitner, and U. Wurstbauer, Control of the orbital character of indirect excitons in MoS_2-WS_2 heterobilayers, Phys. Rev. B **101**, 121404(R) (2020).
[9] B. Laikhtman and R. Rapaport, Exciton correlations in coupled quantum wells and their luminescence blue shift, Phys. Rev. B **80**, 195313 (2009).
[10] A. Griffin, D. W. Snoke, and S. Stringari, *Bose-Einstein Condensation*, revised ed (Cambridge University Press, Cambridge, England, 2010).
[11] A. Gärtner, A. W. Holleitner, J. P. Kotthaus, and D. Schuh, Drift mobility of long-living excitons in coupled GaAs quantum wells, Appl. Phys. Lett. **89**, 052108 (2006).

[12] X. P. Vögele, D. Schuh, W. Wegscheider, J. P. Kotthaus, and A. W. Holleitner, Density Enhanced Diffusion of Dipolar Excitons within a One-Dimensional Channel, Phys. Rev. Lett. **103**, 126402 (2009).
[13] K. Wagner *et al.*, Nonclassical Exciton Diffusion in Monolayer WSe_2, Phys. Rev. Lett. **127**, 076801 (2021).
[14] Z. Sun, A. Ciarrocchi, F. Tagarelli, J. F. Gonzalez Marin, K. Watanabe, T. Taniguchi, and A. Kis, Excitonic transport driven by repulsive dipolar interaction in a van der Waals heterostructure, Nat. Photonics **16**, 1 (2022).
[15] R. Peng *et al.*, Long-range transport of 2D excitons with acoustic waves, Nat. Commun. **13**, 1 (2022).
[16] K. Datta, Z. Lyu, Z. Li, T. Taniguchi, K. Watanabe, and P. B. Deotare, Spatiotemporally controlled room-temperature exciton transport under dynamic strain, Nat. Photonics **16**, 3 (2022).
[17] L. Sigl, F. Sigger, F. Kronowetter, J. Kiemle, J. Klein, K. Watanabe, T. Taniguchi, J. J. Finley, U. Wurstbauer, and A. W. Holleitner, Signatures of a degenerate many-body state of interlayer excitons in a van der Waals heterostack, Phys. Rev. Res. **2**, 042044(R) (2020).
[18] J. P. Eisenstein and A. H. MacDonald, Bose–Einstein condensation of excitons in bilayer electron systems, Nature (London) **432**, 691 (2004).
[19] A. A. High, J. R. Leonard, M. Remeika, L. V. Butov, M. Hanson, and A. C. Gossard, Condensation of excitons in a trap, Nano Lett. **12**, 2605 (2012).
[20] M. Alloing, M. Beian, M. Lewenstein, D. Fuster, Y. Gonzalez, L. Gonzalez, R. Combescot, M. Combescot, and F. Dubin, Evidence for a Bose-Einstein condensate of excitons, EPL Europhys. Lett. **107**, 10012 (2014).
[21] M. Stern, V. Umansky, and I. Bar-Joseph, Exciton liquid in coupled quantum wells, Science **343**, 55 (2014).
[22] X. Liu, K. Watanabe, T. Taniguchi, B. I. Halperin, and P. Kim, Quantum Hall drag of exciton condensate in graphene, Nat. Phys. **13**, 746 (2017).
[23] A. Kogar *et al.*, Signatures of exciton condensation in a transition metal dichalcogenide, Science **358**, 1314 (2017).
[24] Z. Wang, D. A. Rhodes, K. Watanabe, T. Taniguchi, J. C. Hone, J. Shan, and K. F. Mak, Evidence of high-temperature exciton condensation in two-dimensional atomic double layers, Nature (London) **574**, 76 (2019).
[25] G. J. Schinner, J. Repp, E. Schubert, A. K. Rai, D. Reuter, A. D. Wieck, A. O. Govorov, A. W. Holleitner, and J. P. Kotthaus, Confinement and Interaction of Single Indirect Excitons in a Voltage-Controlled Trap Formed Inside Double InGaAs Quantum Wells, Phys. Rev. Lett. **110**, 127403 (2013).
[26] D. N. Shanks *et al.*, Nanoscale trapping of interlayer excitons in a 2D semiconductor heterostructure, Nano Lett. **21**, 5641 (2021).
[27] L. Sigl *et al.*, Optical dipole orientation of interlayer excitons in $MoSe_2 - WSe_2$ heterostacks, Phys. Rev. B **105**, 035417 (2022).
[28] E. Y. Paik, L. Zhang, G. W. Burg, R. Gogna, E. Tutuc, and H. Deng, Interlayer exciton laser of extended spatial coherence in atomically thin heterostructures, Nature (London) **576**, 7785 (2019).
[29] R. Loudon, *The Quantum Theory of Light*, 3rd ed (Oxford University Press, Oxford, New York, 2000).
[30] See Supplemental Material at http://link.aps.org/supplemental/10.1103/PhysRevLett.131.036902 for experimental details on the sample fabrication and optical circuitry with additional figures on the PSF and l_D, which includes Refs. [17,31].
[31] S. Zhao *et al.*, Excitons in mesoscopically reconstructed moiré heterostructures, Nat. Nanotechnol. (2023).
[32] F. Katsch, M. Selig, and A. Knorr, Exciton-Scattering-Induced Dephasing in Two-Dimensional Semiconductors, Phys. Rev. Lett. **124**, 257402 (2020).
[33] C. Lagoin and F. Dubin, Key role of the moire potential for the quasicondensation of interlayer excitons in van der Waals heterostructures, Phys. Rev. B **103**, L041406 (2021).
[34] M. Bieniek, K. Sadecka, L. Szulakowska, and P. Hawrylak, Theory of excitons in atomically thin semiconductors: Tight-binding approach, Nanomater. Nanotechnol. **12**, 9 (2022).
[35] M. M. Glazov, Z. A. Iakovlev, and S. Refaely-Abramson, Phonon-induced exciton weak localization in two-dimensional semiconductors, Appl. Phys. Lett. **121**, 192106 (2022).
[36] M. Selig, G. Berghäuser, M. Richter, R. Bratschitsch, A. Knorr, and E. Malic, Dark and bright exciton formation, thermalization, and photoluminescence in monolayer transition metal dichalcogenides, 2D Mater. **5**, 035017 (2018).
[37] B. Remez and N. R. Cooper, Leaky exciton condensates in transition metal dichalcogenide moiré bilayers, Phys. Rev. Res. **4**, L022042 (2022).
[38] S. Dietl, S. Wang, D. Schuh, W. Wegscheider, J. P. Kotthaus, A. Pinczuk, A. W. Holleitner, and U. Wurstbauer, Collective electronic excitation in a trapped ensemble of photogenerated dipolar excitons and free holes revealed by inelastic light scattering, Phys. Rev. B **95**, 085312 (2017).